OPEN ACCESS
IOP Publishing
Journal of Physics D: Applied Physics
J. Phys. D: Appl. Phys. **50** (2017) 415206 (13pp)
https://doi.org/10.1088/1361-6463/aa8519

Self-stabilized discharge filament in plane-parallel barrier discharge configuration: formation, breakdown mechanism, and memory effects

R Tschiersch[1], S Nemschokmichal[1], M Bogaczyk[2] and J Meichsner[1]

[1] Institute of Physics, University of Greifswald, Felix-Hausdorff-Str. 6, 17489 Greifswald, Germany
[2] Leibniz Institute for Plasma Science and Technology, Felix-Hausdorff-Str. 2, 17489 Greifswald, Germany

E-mail: robert.tschiersch@uni-greifswald.de

Received 12 May 2017, revised 21 July 2017
Accepted for publication 9 August 2017
Published 21 September 2017

Abstract

Single self-stabilized discharge filaments were investigated in the plane-parallel electrode configuration. The barrier discharge was operated inside a gap of 3 mm shielded by glass plates to both electrodes, using helium-nitrogen mixtures and a square-wave feeding voltage at a frequency of 2 kHz. The combined application of electrical measurements, ICCD camera imaging, optical emission spectroscopy and surface charge diagnostics via the electro-optic Pockels effect allowed the correlation of the discharge development in the volume and on the dielectric surfaces. The formation criteria and existence regimes were found by systematic variation of the nitrogen admixture to helium, the total pressure and the feeding voltage amplitude. Single self-stabilized discharge filaments can be operated over a wide parameter range, foremost, by significant reduction of the voltage amplitude after the operation in the microdischarge regime. Here, the outstanding importance of the surface charge memory effect on the long-term stability was pointed out by the recalculated spatio-temporally resolved gap voltage. The optical emission revealed discharge characteristics that are partially reminiscent of both the glow-like barrier discharge and the microdischarge regime, such as a Townsend pre-phase, a fast cathode-directed ionization front during the breakdown and radially propagating surface discharges during the afterglow.

Keywords: barrier discharge, microdischarge, patterned discharge, glow-like discharge, surface charge, memory effect, gap voltage

(Some figures may appear in colour only in the online journal)

1. Introduction

Atmospheric-pressure barrier discharges (BDs) typically operate in the microdischarge (MD) regime, which is characterized by arbitrarily distributed filament-like breakdowns on the nanosecond time scale. Unlike the controlled operation of laterally diffuse BDs, which has been possible for the last three decades [1–3], MDs in atmospheric air have already been used since the 19th century in ozone generators, e.g. for the disinfection of drinking water [4, 5]. Due to the dielectric-covered electrodes, the transition to arc discharges is avoided, and non-equilibrium plasmas are generated even at elevated pressures. Thereby, a variety of reactive species is provided, such as hot electrons, radicals and photons in the VIS and UV range [6–8]. Nowadays, further applications benefit from the high chemical reactivity at a low gas temperature, especially

the surface treatment of heat-sensitive materials in biology and medicine [9, 10]. Recently, the immense potential of BDs for life-science has received significant attention.

Although MDs have been known for long time and have extensively been used for applications, the discharge mechanism was first well understood when sophisticated diagnostic tools were accessible. The MD breakdown is strongly determined by a high ionization rate and a significant space charge formation in the volume, as well as by the interaction between the discharge species and the electrically charged dielectric-covered electrodes. Hence, both diagnostics of the volume and surface processes under identical discharge conditions are needed for a comprehensive description.

High-quality investigations of the discharge development in the volume became possible by cross-correlation spectroscopy based on single-photon counting [11–13], and streak camera imaging [14–16], both providing a high sensitivity and sub-nanosecond resolution. In particular, the spectral as well as spatio-temporal measurement of the optical emission in combination with a collision-radiation model enabled the determination of the two-dimensional electric field development during MD breakdown. Three characteristic phases were identified: (i) Townsend pre-phase of μs duration, (ii) fast cathode-directed streamer marking the breakdown on the ns time scale and (iii) radially propagating surface discharges during the post-phase. However, these optical diagnostics require accumulation over many discharge cycles. Therefore, the investigation of the volume discharge has been restricted to semi-spherical electrodes that allow us to localize the periodic breakdown of a single MD. Besides, multi-dimensional simulations indicate the role of the photo-ionization and photo effect for the fast streamer propagation, and the importance of residual surface charges for the localized discharge re-ignition [17–20].

Besides the indication of the surface charges and their binding energies by thermally or optically stimulated current and thermoluminescence measurements [21–23], fundamental knowledge about the influence of surface charges on BD mechanisms has foremost been achieved by a diagnostic technique based on the electro-optic Pockels effect of a bismuth silicon oxide ($Bi_{12}SiO_{20}$) crystal [24–26]. The surface charge memory effect was qualitatively proved for the re-ignition behavior of multiple MDs [27, 28] and for the long-term stabilization of laterally patterned BDs [30, 31]. It was shown that positive and negative surface charges accumulate in Gaussian profiles on the dielectrics as the footprints of a filamentary breakdown. This favors the conservation of the breakdown position due to the local enhancement of both the electric field across the gas gap and the effective secondary electron emission. Moreover, the decay and lateral transport of surface charges happens on the second to minute time scale, which clearly exceeds the typical discharge cycle [28, 32]. However, this powerful diagnostic tool is restricted to plane electrode configurations.

Despite the scope of knowledge gained during the last few decades using complementary electrode configurations, the investigation of MDs in the volume as well as on the dielectric surfaces using one configuration and identical conditions is still missing. That is why the present work is focused on the comprehensive characterization of a single self-stabilized discharge filament in the plane-parallel electrode configuration. It allowed the combined application of electrical, optical and surface charge diagnostics. In this context, the helium-nitrogen mixture, the total pressure and the feeding voltage amplitude were systematically varied in order to study the formation and stabilization criteria and related existence regimes. As a highlight, the breakdown mechanism in the volume was correlated with the surface charge dynamics on the dielectrics.

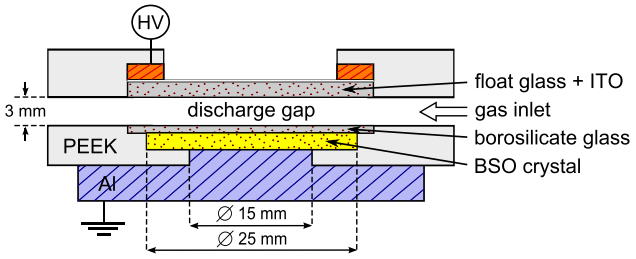

Figure 1. Sketch of the discharge configuration from the side-view.

The outline of this article is as follows. The experimental setup and the diagnostics are briefly introduced in section 2. Section 3 presents the formation procedure to obtain single self-stabilized discharge filaments. Section 4 is focused on the correlation of the discharge development in the volume and on the dielectric surfaces. Finally, the importance of the volume and surface memory effects for the self-stabilization of the discharge filament is discussed in section 5.

2. Experimental setup and diagnostics

2.1. Discharge configuration

A sketch of the plane-parallel discharge configuration is depicted from the side-view in figure 1. The high-voltage driven copper ring was connected with the electrically conductive and optically transparent indium tin oxide (ITO) layer coated on a float glass plate (thickness of 0.7 mm, permittivity of 7.6). The bismuth silicon oxide ($Bi_{12}SiO_{20}$) crystal (thickness of 0.7 mm, permittivity of 56) was placed on the grounded aluminum mirror and allows the measurement of surface charges via the electro-optic Pockels effect. As a new feature compared to previous investigations [27, 28], the surface charge diagnostics were extended to common transparent dielectrics covering the BSO crystal, as reported in [29]. In the present experiment, borosilicate glass (thickness of 0.2 mm, permittivity of 6.7) was used, resulting in the most symmetric discharge behavior comparing both half-cycles of the applied voltage. The discharge gap was set to 3 mm by insulating gap spacers made of polyether ether ketone (PEEK).

2.2. Vacuum system and gas supply

The discharge cell was placed inside a vacuum chamber made of stainless steel. The chamber was evacuated to a base pressure below 10^{-5} mbar before the operating gas was directly supplied into the discharge volume. Well-defined helium-nitrogen

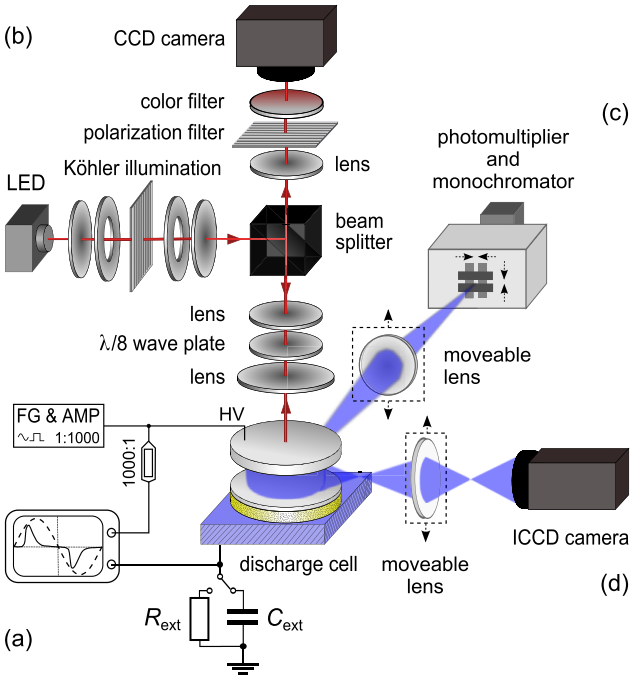

Figure 2. Setup of the diagnostics: (a) electrical measurements, (b) surface charge diagnostics, (c) optical emission spectroscopy and (d) ICCD camera imaging.

mixtures with a respective purity of >99.999% were realized by adjusting the gas flow rates using two mass flow controllers. The total flow rate was 100 sccm. Note that it was possible to add oxygen in the same way. The total pressure was varied between 100 mbar and 1 bar and then kept constant in the flowing regime by a diaphragm pressure gauge (MKS) in combination with a butterfly valve (MKS) and a process pump (TRIVAC D25BCSPFPE).

2.3. Electrical measurements

The diagnostic setup in figure 2 allowed the simultaneous application of (a) electrical measurements, (b) surface charge diagnostics, (c) optical emission spectroscopy and (d) ICCD camera imaging at one electrode configuration under identical conditions.

The square-wave feeding voltage $U_{ext}(t)$ at the frequency of 2 kHz was provided by a function generator (SRS DS345) in combination with a voltage amplifier (Trek 615-10, amplification of 1:1000), measured via a HV probe (Tektronix P6015A, 1000:1), and connected to the upper electrode. Applying a square-wave signal, the amplifier provides a voltage slope of about $\pm 250\,\mathrm{V}\ \mu\mathrm{s}^{-1}$, see also [29]. Moreover, the total transported charge $Q_{ext}(t)$ was measured via an external capacitor ($C_{ext} = 1.2$ nF). The signals were processed by a digital oscilloscope (ROHDE&;SCHWARZ RTO1024). Based on the equivalent circuit introduced in [33], the spatially averaged gap voltage

$$U_{gap}(t) = \left(1 + \frac{C_{par}}{C_{die}}\right) U_{ext}(t) - \frac{1}{C_{die}} Q_{ext}(t), \qquad (1)$$

the actual discharge current without the displacement current through the dielectrics and the gas gap,

$$I_{dis}(t) = \left(1 + \frac{C_{gap}}{C_{die}}\right)\left(\frac{\mathrm{d}Q_{ext}(t)}{\mathrm{d}t} - C_{tot}\frac{\mathrm{d}U_{ext}(t)}{\mathrm{d}t}\right) \qquad (2)$$

and the time-integral of the discharge current, which corresponds to the surface charge dynamics

$$Q_{sur}(t) = \left(1 + \frac{C_{gap}}{C_{die}}\right)\left(Q_{ext}(t) - C_{tot}\, U_{ext}(t)\right), \qquad (3)$$

were calculated. Here, C_{gap} and C_{die} are the calculated capacitances of the discharge gap and the dielectrics, respectively. Moreover, C_{tot} is the total capacitance determined from the flat slope of the $Q_{ext}(U_{ext})$ plot, and $C_{par} = C_{tot} - C_{gap}C_{die}/(C_{gap} + C_{die})$ considers the surroundings beyond the lateral discharge area.

2.4. Surface charge diagnostics

Surface charges were measured via the electro-optic Pockels effect of the BSO crystal. Figure 2(b) shows the optical setup. First, the LED light ($\lambda = 634$ nm) was homogenized by passing the Köhler illumination system and then it was diverted in the direction of the discharge cell by a linearly polarizing beam splitter. Following this path, the LED light became elliptically polarized by a $\lambda/8$ wave plate, expanded by a telescopic system, and finally passed the discharge cell twice, due to the reflection at the grounded aluminum mirror. Finally, the light intensity was detected by a CCD camera (Miro 4ex). During the discharge operation, the voltage drop across the BSO crystal, caused by the deposited surface charges (U^{σ}_{BSO}) and the applied voltage (U^{ext}_{BSO}), induces a birefringence and thus an additional change in the polarization of the LED light. As a result, the detected light intensity depends on the amount and polarity of the deposited surface charge. The final formula for the calculation of the spatio-temporally resolved surface charge density reads

$$\sigma_{sur}(x,y,t) = \frac{\varepsilon_0\varepsilon_{BSO}}{d_{BSO}}\left(\frac{I_{meas}}{I_{ref}} - 1\right)\left(U^{ext}_{BSO} + \frac{1}{2k}\right). \qquad (4)$$

Here, ε_0, ε_{BSO} and d_{BSO} are the electric field constant and the permittivity and thickness of the BSO crystal, respectively. $I_{meas}(U^{ext}_{BSO}, U^{\sigma}_{BSO})$ denotes the measured intensity during the discharge operation. The reference intensity $I_{ref}(U^{ext}_{BSO})$ without any discharge is obtained from a calibration measurement. The proportionality factor k is determined from the linear dependence of I_{ref} on U^{ext}_{BSO}. Further details are given in [27, 29].

Moreover, the measurement of the surface charge density distribution with respect to the phase of the feeding voltage $U_{ext}(t)$ allowed the calculation of the spatio-temporally resolved gap voltage

$$U_{gap}(x,y,t) = \frac{C^{px}_{die}}{C^{px}_{die} + C^{px}_{gap}} U_{ext}(t) - \frac{A^{px}}{C^{px}_{die}}\,\sigma_{sur}(x,y,t). \qquad (5)$$

Here, the observation area detected per pixel of the CCD camera chip was $A^{px} = 4\ \mathrm{x}\ 10^{-5}\ \mathrm{cm}^2$. Especially in the case of a filamentary barrier discharge, the gap voltage changes drastically over the electrode area.

2.5. Optical emission spectroscopy

The optical emission from the discharge was depicted by a vertically moveable lens onto the entrance slit of a monochromator (Acton Research Corporation, SpectraPro, focal length of 750 mm) and detected by a photomultiplier tube (Hamamatsu R928). By means of a 1800^{-1} mm grating, a spectral resolution of 0.5 nm was achieved. A horizontal slit (0.1 mm width) was placed in front of the monochromator and the lens was moved in steps of 0.05 mm, which allowed the axial scan of the discharge gap width of 3 mm. The digital oscilloscope recorded the photomultiplier signal with a temporal resolution down to 10 ns.

2.6. ICCD camera imaging

In addition, the discharge volume was depicted using a gated intensified charge-coupled device (ICCD) camera (Princeton Instruments PI-MAX). The 1:3 imaging via an external lens onto the camera chip (512×512 pixel and 0.12 mm/pixel spatial resolution) provided an effective spatial resolution of 0.04 mm. The maximum temporal resolution of 1 ns allowed fast 2D imaging of the filamentary discharge breakdown.

3. Operation of a single discharge filament

3.1. Formation procedure

Two different procedures were identified that allow the formation of single self-stabilized discharge filaments. First, after the He/N_2 discharge was already operated in the micro-discharge (MD) regime, the reduction of the feeding voltage amplitude leads to the stabilization of several self-organized discharge filaments. Finally, a single self-stabilized discharge filament remains. This procedure is shown in figure 3(a) by discharge current profiles and photographs from the side-view (averaged over ten voltage periods) of the filamentary discharge in He with 10 vol.% N_2 admixture at the total pressure of 1 bar. Here, most notable is the transition from the non-stationary MD current pulses of about 100 ns duration at 3.2 kV to one stable current pulse of about 1 μs duration for several synchronously occurring discharge filaments at 2.6 kV. The simultaneous ignition of the discharge filaments is characteristic for patterned BDs usually operated at lower pressures [30, 31, 34]. This is favored by the steep slope of the square-wave feeding voltage (or high-frequency sine-wave feeding voltage) and by similar charge amounts deposited by each of the discharge filaments. Due to the comparatively slow discharge development on the microsecond time scale, the desorption of electrons from the cathodic dielectric by the initial photons might trigger multiple discharge events [35]. Moreover, the photographs indicate the arbitrary distribution of MDs at 3.2 kV and an axial discharge structure, as well as broadened footprints on the dielectrics in the case of the self-stabilized discharge filaments at 2.6 kV and 2.2 kV. Note that the single discharge filament operates at a voltage amplitude that is about 1 kV lower than the initial ignition voltage. It indicates that the residual surface charges significantly

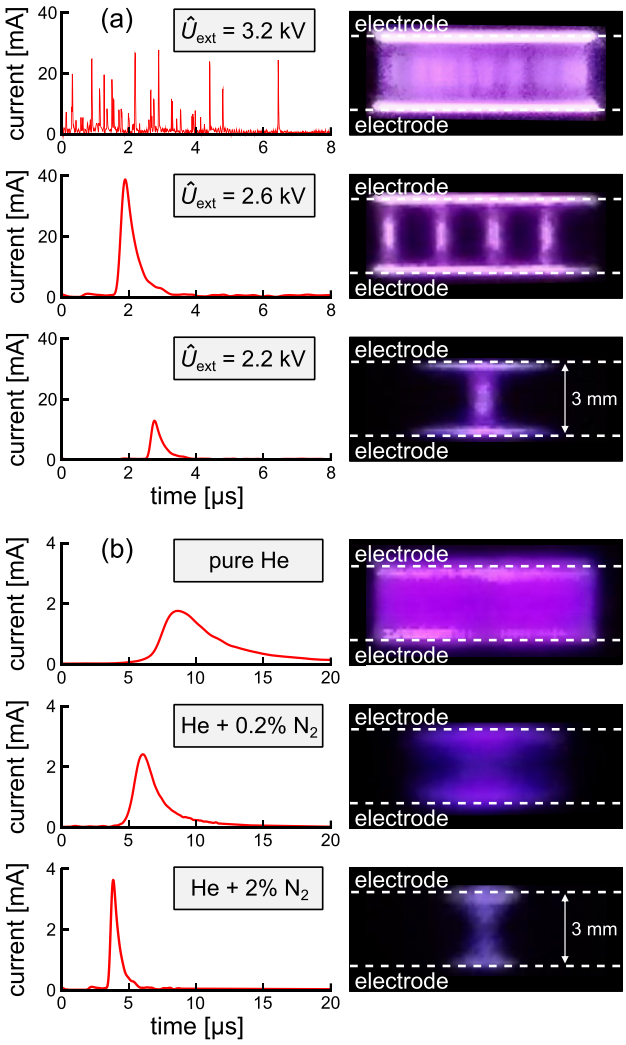

Figure 3. Formation procedures for single self-stabilized discharge filaments: discharge current and photographs from the side-view (averaged over ten voltage periods) of the square-wave driven discharge in (a) He with 10 vol.% N_2 admixture at a pressure of 1 bar for different feeding voltage amplitudes $\hat{U}_{ext}$ and (b) He with different N_2 admixtures at a pressure of 500 mbar and a feeding voltage amplitude of $\hat{U}_{ext} = 0.8$ kV.

contribute to the effective electric field across the gas gap. Hence, the local surface charge distribution seems to be the key for understanding the self-stabilization of discharge filaments at low voltage amplitudes.

The second procedure is starting from the diffuse glow-like discharge in helium at a fixed total pressure of 500 mbar and a feeding voltage amplitude of 0.8 kV. As shown in figure 3(b), admixing at least 0.2 vol.% N_2 to He leads to the constriction of the diffuse discharge in a lateral direction and, finally, to the formation of a single self-stabilized discharge filament. Following this mode transition, the discharge current maximum rises but the pulse duration decreases, again ending up with the typical characteristics of a single discharge filament as described above. It is striking that the breakdown onset is shifted to earlier times with increasing N_2 admixture to He at otherwise equal feeding voltage amplitude, which indicates an enhanced pre-ionization. The admixture of N_2 enhances the effective ionization coefficient α_{eff} due to the

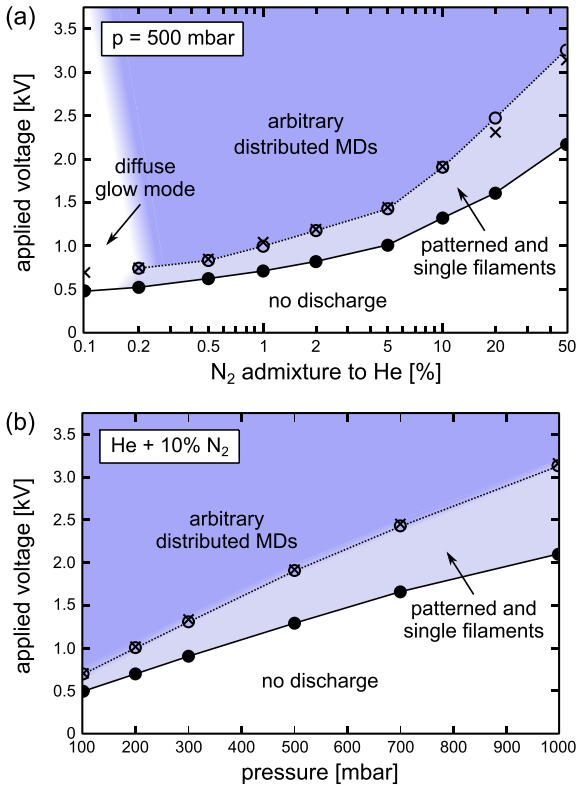

Figure 4. Existence of diffuse and filamentary discharge modes depending on both the applied voltage amplitude and (a) the N_2 admixture to He at a fixed total pressure of 500 mbar and (b) the total pressure at a fixed gas mixture of He with 10 vol.% N_2. The crosses and the filled or empty circles mark the initial ignition voltage, the minimum voltage for maintaining the discharge and the mode transition voltage, respectively.

Penning ionization of N_2 via He metastable states [29, 36, 37]. This process favors the space charge formation and the corresponding electric field distortion, but it is too slow to initiate streamer breakdown. In turn, the increase in effective ionization is associated with the decrease in radius of the charge carrier avalanches, $r \approx \alpha_{\mathrm{eff}}^{-1}$ in first approximation, which may explain the constriction of the discharge.

3.2. Existence regimes

After the discussion of exemplary parameter sets allowing the formation of single self-stabilized discharge filaments, in the following, the existence regimes are presented, which were obtained by systematic variation of the He/N_2 mixture, total pressure and feeding voltage amplitude. In figure 4(a), the existence of diffuse and filamentary discharge modes is plotted depending on the feeding voltage amplitude and the N_2 admixture to He. Here, the total pressure was fixed to 500 mbar in order to limit the applied voltage that is necessary for the discharge operation at large N_2 admixtures. As is well known, the diffuse glow-like BD occurs in pure He, as well as in He with small N_2 additives at moderate voltage amplitudes. However, at larger N_2 admixtures and at over-voltage indicated by open circles, the discharge is initially operated in the MD regime. When the feeding voltage is reduced after the initial discharge ignition, stable filament patterns and, near to critically low voltage amplitudes marked by solid circles, single discharge filaments can be operated over a wide range of the N_2 admixture. Once a sufficient ionization rate caused the filamentation of the discharge by admixing at least about 0.2 vol.% N_2 to He, the stabilization mechanism of the discharge filaments seems to be independent of the gas system. The transition region between the MD regime and self-organized discharge filaments is characterized by the superposition of a few MDs and a rotating filament pattern. The associated transition voltage resulting only in MDs is indicated by crosses and, however, is sharply defined. It does not reveal a significant hysteresis with respect to the initial ignition voltage for MDs marked by open circles.

Moreover, in figure 4(b), the existence diagram is plotted by the feeding voltage amplitude versus the total pressure between 100 mbar and 1 bar. Here, the admixture of 10 vol.% N_2 to He was fixed, which allows the formation of stable discharge filaments. Just as observed for the variation of the N_2 admixture, stable filaments can be operated below the initial ignition voltage over the entire range of total pressure, which again proves the independence of the stabilization mechanism from specific gas properties. Note that the voltage interval for the patterned and single discharge filaments increases from $\Delta U_{\mathrm{ext}} \approx 0.3$ kV at 100 mbar to $\Delta U_{\mathrm{ext}} \geqslant 1$ kV at 1 bar, which is the same trend as for the increasing N_2 admixture in figure 4(a). This is an indication of the outstanding importance of the residual surface charge, which increases with rising pressure and N_2 admixture, for the localized re-ignition of discharge filaments and thus for their long-term stability.

Figure 5 shows the influence of (a) the N_2 admixture to He and (b) the total pressure on the spatial dimensions of a single self-stabilized discharge filament based on averaged photographs from the side-view. In (a), the total pressure of 500 mbar was fixed and the feeding voltage was close to the respective maintaining voltage in figure 4(a). For increasing N_2 admixture from up to 50 vol.%, the average diameter of the discharge channel does not remarkably change, but the lateral extent of surface discharges on both dielectrics increases significantly. Note that the overall extent of the surface discharges at 50 vol.% N_2 additive could not be recorded, due to the limitations of the orifice into the discharge cell. Thus, it is indicated by a dashed line reflecting the recorded side. Indeed, the same characteristics are observed for the rising total pressure in (b). Here, the admixture of 10 vol.% N_2 to He was fixed and the operating voltage is associated with the existence regime in figure 4(b). Both with increasing N_2 admixture and total pressure, the amount of transported and subsequently deposited charge increases as well. Since the average channel diameter keeps nearly constant, the localized increase in the surface charge amount causes a larger electric field gradient in the lateral direction and, thereby, the larger extent of the following surface discharges. Not least due to the averaging over several discharge cycles, the photographs in figure 5 only allow the rough estimation of the filament diameter in the sub-millimeter range. For comparison, detailed investigations on the streamer breakdown in nitrogen and argon revealed a

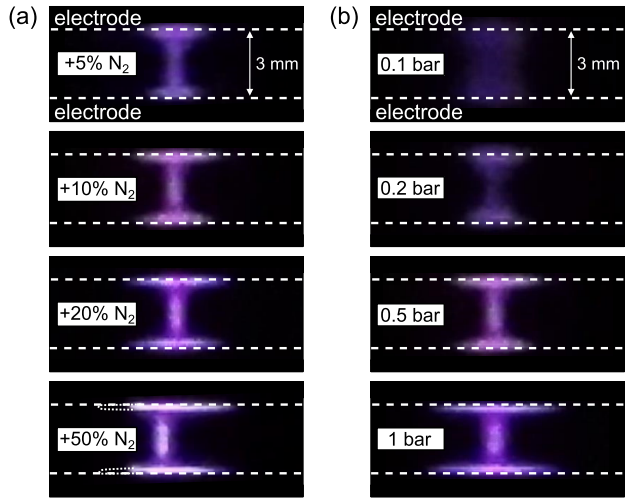

Figure 5. Photographs from the side-view (averaged over ten voltage periods) of a self-stabilized discharge filament: (a) for different N_2 admixtures to He within the corresponding existence regime in figures 4(a) and (b) for different total pressures within the corresponding existence regime in figure 4(b).

changing diameter between about 50 μm and 150 μm along the symmetry axis of the discharge filament [38].

4. Discharge development

4.1. Townsend pre-phase

After the phenomenological description, now the focus is on the discharge physics starting with the pre-phase. In figure 6, the applied voltage $U_{\mathrm{ext}}(t)$, the averaged gap voltage $U_{\mathrm{gap}}(t)$, the discharge current $I_{\mathrm{dis}}(t)$ (top) and the spatio-temporal evolution of the He emission at 706.5 nm (bottom) are depicted during the pre-phase of the self-stabilized discharge filament operated in He with 10 vol.% N_2 at atmospheric pressure. The gap voltage clearly exceeds the applied voltage, due to the additional electric field caused by residual surface charges. Since the discharge current rises gradually, there is still no significant space charge formation and corresponding distortion of the electric field, wherefore this phase is referred to as the Townsend pre-phase. The microsecond time scale of the pre-phase clearly exceeds the effective lifetime of the radiative He(3^3S) state that is dominantly populated by electron-impact. Thus, the measured He($3^3S \rightarrow 2^3P$) emission intensity follows the electron density profile

$$n_{\mathrm{e}}(z) = n_{\mathrm{e}}(z=0)\exp[\alpha_{\mathrm{eff}}(E/n)z]. \qquad (6)$$

Starting at the cathode with $n_{\mathrm{e}}(z=0)$, the electron density $n_{\mathrm{e}}(z)$ rises exponentially towards the anode, according to the effective ionization coefficient α_{eff} that is determined by the reduced electric field strength E/n. At a fixed time during the Townsend pre-phase, the electric field across the gas gap is approximately constant. Fitting the axial profile of the He emission according to equation (6) yields $\alpha_{\mathrm{eff}} = 4.2(2)\ \mathrm{mm}^{-1}$ as the average value for the temporal window between 253.5 μs and 254.5 μs. The increase in gap voltage during this temporal window causes no remarkable trend in α_{eff}, hence the change is smaller than the standard deviation. The ionization factor $\alpha_{\mathrm{eff}} \times g$ at the anode ($z = g = 3$ mm) yields 12–13. While coming closer to the breakdown, the growing space charge and corresponding enhancement of the local electric field may result in the critical value of $\alpha_{\mathrm{eff}} \times g \approx 18$–20 that is necessary for streamer breakdown according to Meek's criterion. Besides, a Townsend pre-phase of μs duration was also observed for the MD regime in air [12, 16], as well as for the glow-like BD in He [29].

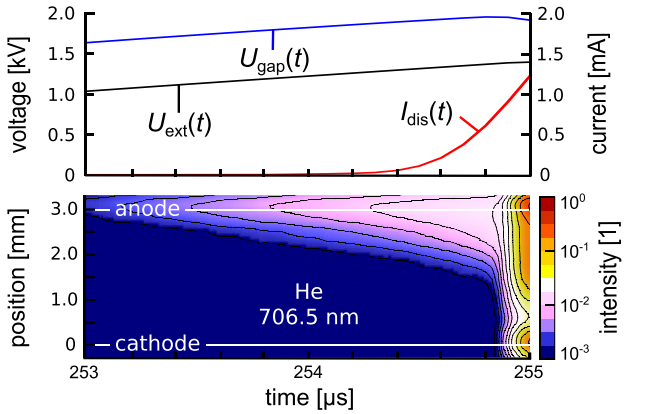

Figure 6. Townsend pre-phase of the self-stabilized discharge filament. Top: feeding voltage $U_{\mathrm{ext}}(t)$, average gap voltage $U_{\mathrm{gap}}(t)$ and discharge current $I_{\mathrm{dis}}(t)$. Bottom: spatio-temporal evolution of the He emission at 706.5 nm. Operating conditions: He with 10 vol.% N_2, $p = 1$ bar, $\hat{U}_{\mathrm{ext}} = 2.5$ kV.

4.2. Breakdown mechanism

Figure 7 shows the ICCD camera images from the side-view at different times (a)–(i) (indicated above) during the development of two self-stabilized discharge filaments operating in He with 10 vol.% N_2 additive at a pressure of 1 bar. The exposure time of the camera was set to 2 ns, whereas the temporal jitter of the discharge comparing consecutive voltage periods was up to 10 ns. Note that the breakdown onset is influenced by small deviations in the residual surface charge amount and by the statistical time of effective electron generation. However, due to the overall sub-μs time scale of the discharge development, the characteristic discharge phases could be separated despite this temporal jitter.

First, the Townsend pre-phase is well-localized, as indicated by the weak optical emission in front of the anode (a), (b). Then, when a critical space charge has built up in front of the anode, a thin ionization channel closes across the gas gap (c). The propagation of the cathode-directed ionization front is faster than the temporal jitter of the discharge up to 10 ns, which is similar to the streamer propagation of a micro-discharge breakdown reaching velocities of 1 mm $\times$ ns^{-1} [12, 15, 16]. It is striking that one of the two discharge filaments ignites some tens of nanoseconds earlier. Most likely, small deviations in the amounts of deposited surface charges or in the gas flow rate influence the discharge re-ignition behavior. As already mentioned, the first breakdown might

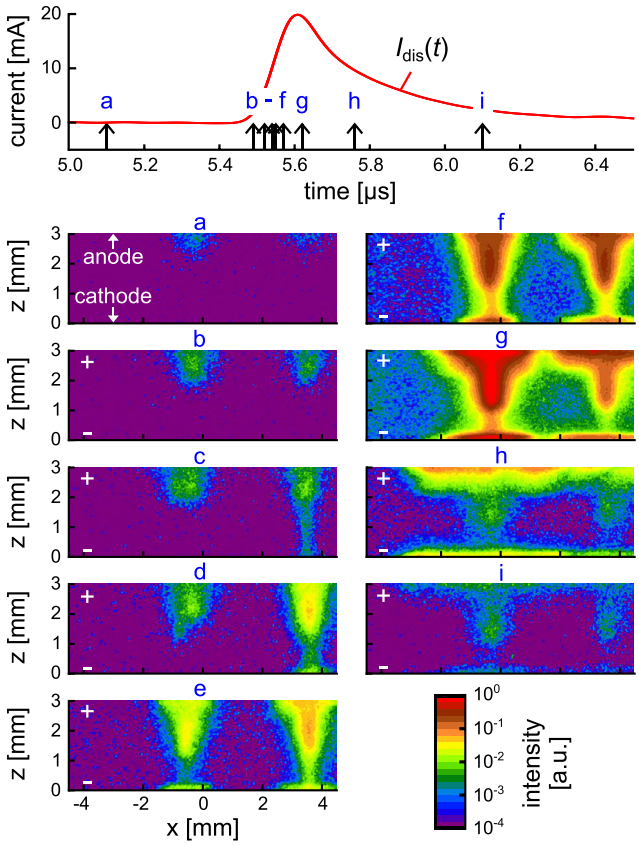

Figure 7. Spatio-temporal development of two self-stabilized discharge filaments: discharge current profile and ICCD camera imaging from the side-view (temporal resolution of 2 ns) at different times a–i indicated above. Operating conditions: He with 10 vol.% N_2, $p = 1$ bar, $\hat{U}_{ext} = 2.4$ kV.

trigger the second one by the photo-desorption of surface electrons [35]. Once the initial ionization channel has formed, an axial structure builds up that is typical for the glow-like discharge until the current maximum is reached, (d)–(g). Starting at the cathode, a negative glow is followed by Faraday dark space, a positive column and anode glow [39]. At this time, a weak optical emission intensity is recorded in the surrounding regions too, which indicates the presence of electrons there. Finally, the discharge post-phase is characterized by a long-lasting optical emission inside the discharge channel and radially propagating surface discharges on both dielectrics, (g)–(i). Again, the surface discharges are typical for the MD development.

In figure 8, Abel inversion of the ICCD camera images allows us a closer look at the radial development of the surface discharges during the afterglow. Note that the discharge conditions are exactly the same as in figure 7. The lateral propagation is annular on the cathodic dielectric. Here, the constricted ionization front accumulates positive surface charges resulting in a high lateral electric field gradient. Note that the surface discharge on the anodic dielectric is slightly slower and lasts noticeably longer. Most likely, this is due to the wider accumulation of negative surface charges, which does not cause as high electric field gradients as on the cathodic dielectric.

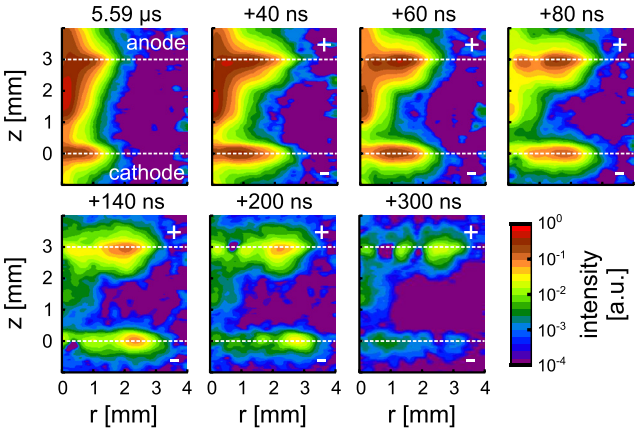

Figure 8. Spatio-temporal development of surface discharges during the post-phase of a self-stabilized discharge filament shown by Abel inversion of ICCD camera images. Operating conditions: He with 10 vol.% N_2, $p = 1$ bar, $\hat{U}_{ext} = 2.4$ kV.

4.3. Electric field development

Figure 9 shows (a) the discharge current profile, (b) the spatio-temporal evolution of the He emission at 706.5 nm and (c) the intensity ratio of the He emission at 667.8 nm and 728.1 nm during the breakdown of the self-stabilized discharge filament. The He emission in (b) reveals the Townsend pre-phase, the negative glow, Faraday dark space, positive column and anode glow at the maximum discharge current, as well as the long-lasting afterglow. Note that the anode glow is even more intensive than the negative glow. Except the filamentary appearance and the surface discharges on the dielectrics, the similarities are obvious between the breakdown mechanisms of a self-stabilized discharge filament in He/N_2 mixtures and the diffuse glow-like BD typically operating in nominally pure He.

From the literature, it is known [40] that the ratio between the intensities of the He singlet transitions at 667.8 nm and 728.1 nm in figure 9(c) is a measure of the local electric field, if the predominant population of the corresponding radiative states He(3^1D) and He(3^1S) by electron-impact excitation from the He ground state is ensured. First, collisional-induced conversion from the metastable singlet state He(2^1S) to the slightly less energetic metastable triplet state He(2^3S) is much more efficient than vice versa. Second, both metastable states are effectively quenched by nitrogen molecules via Penning ionization, according to the rate coefficient $k_{PI} = 5 \times 10^{-11}$ cm^3 s^{-1} [37]. The additive of 10 vol.% N_2 to He at the total pressure of 1 bar corresponds to a nitrogen density of $n_{N_2} \approx 2 \times 10^{18}$ cm^{-3}. Under these conditions, the lifetime of He metastable states is $\tau_{He^m} \approx (k_{PI} n_{N_2})^{-1} \approx 10$ ns. Hence, electron-impact excitation from the metastable single state He(2^1S) to the radiative states He(3^1D) and He(3^1S) is negligible.

As can be seen in figure 9(c), during the late discharge pre-phase, the intensity ratio and thus the electric field is slightly enhanced near the anode, which indicates the positive space charge formation. Afterwards, the propagation of the ionization front occurs within the temporal discharge jitter, but a

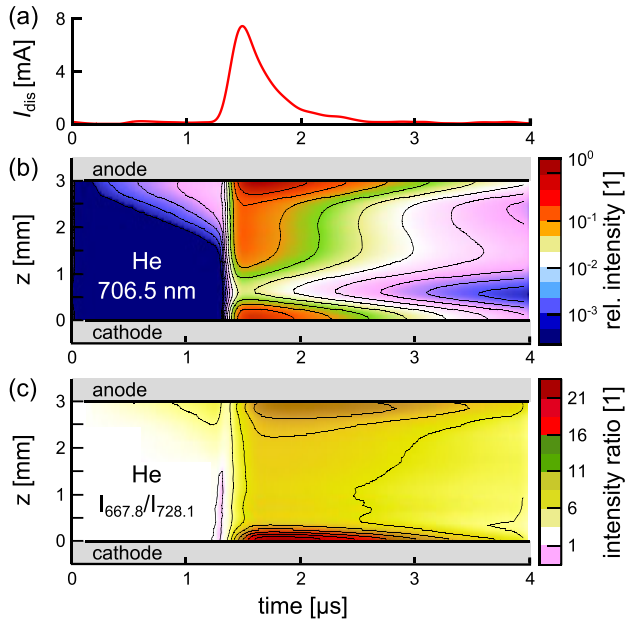

Figure 9. Breakdown characteristics of a single self-stabilized discharge filament: (a) discharge current, (b) spatio-temporally resolved He emission at 706.5 nm, and (c) intensity ratio of He emission at 667.8 nm and 728.1 nm. Operating conditions: He with 10 vol.% N_2, $p = 1$ bar, $\hat{U}_{ext} = 2.5$ kV.

closer look reveals the cathode-directed development ending up with a global maximum. This significant enhancement of the electric field at the moment of the discharge current maximum indicates the cathode fall region that is most characteristic of the glow-like BD. At the same time, the electric field within the positive column is clearly lower and almost constant, as known from simulations of the BD in He [39]. The local maximum at the anode is delayed with respect to the global maximum at the cathode. Note that the measurement does not distinguish between the axial and lateral electric field components. Consequently, both the long-lasting global maximum and local maximum indicate high lateral electric field gradients, due to well-localized surface charge spots, which cause the propagation of surface discharges on both dielectrics. Note that the surface discharge on the anodic dielectric is slower and lasts longer, as revealed by the Abel inversion of the ICCD camera images in figure 8.

4.4. Surface charge dynamics

After the discussion of the discharge development in the volume from the side-view, the correlated surface charge dynamics is presented. Figure 10(a) depicts the accumulation of positive surface charges onto the cathodic dielectric during the breakdown of a single self-stabilized discharge filament operated in He with 10 vol.% N_2 at a pressure of 1 bar and a feeding voltage amplitude of 2.2 kV. Below, the surface charge density distribution is shown and the 1D profile through the maximum of the surface charge spot is plotted above.

During the discharge pre-phase, residual surface electrons are present on the cathodic dielectric. Their material-dependent binding energy is in the order of 1 eV [21, 22]. That is why surface electrons can be easily released and may support the pre-ionization. Actually, no decreasing trend in the surface electron density is identified during the pre-phase, however, the resolution is about 0.05 nC cm^{-2}. Note that even a very small amount of 10 pC additional electrons is able to significantly enhance the pre-ionization in He barrier discharges, as revealed by a laser-photodesorption experiment in combination with a fluid simulation [41]. As already known from previous studies [27, 28], surface charges form Gaussian profiles at the footprint of MD channels. The density profile of negative surface charges has a minimum of about $\sigma_- = -3$ nC cm^{-2} and a full width at half maximum of about $\omega_- = 6.0$ mm. The latter is large compared to 1.6 mm observed for MDs in nitrogen [27]. Assuming the Gaussian distribution, the overall charge amount is about $Q_{sur} = \pi\sigma_-\omega_-^2/2 = -1.7$ nC. Once the breakdown has started at 5.4 μs in figure 10(a), positive surface charges are accumulating on the cathodic dielectric. In more detail, the positive ions, coming along with the constricted ionization front, hit the cathodic dielectric at the center of the negative surface charge spot. Thereby, a ring of residual surface electrons remains during the breakdown between 5.6 μs and 5.7 μs. According to the ICCD camera image (g) in figure 7, the cathodic footprint of the discharge channel has a lateral extent of about 3 mm. This correlates well with the inner diameter of the surface electron ring. The centered formation of the positive surface charges was also observed for the patterned BD in He/N_2 mixtures at significantly lower pressures [31].

Complementarily, the deposition of negative surface charges onto the anodic dielectric is shown in figure 10(b). In this case, the subsequent half-period of the feeding voltage was recorded, due to the restriction of the surface charge diagnostics to the bottom electrode that is covered with the BSO crystal. The Gaussian profile of the positive surface charge just before the breakdown onset differs significantly from the negative profile already described, compare figure 10(a) at 5.4 μs with figure 10(b) at 255.3 μs. The amplitude is about 6 nC cm^{-2} and thus twice as large, but the full width at half maximum is smaller and amounts to 4.8 mm. The overall charge results in 2.2 nC. The discrepancy to the negative charge amount (−1.7 nC) was already pointed out in previous investigations [27, 29]. Most likely, it indicates a bias caused by different secondary electron emission coefficients of the dielectrics used [42]. During the breakdown phase, the wide deposition of surface electrons on the anodic dielectric is revealed, unlike the centered accumulation of positive surface charges on the cathodic dielectric resulting in a ring of residual surface electrons. Note that the low-pressure patterned BD also shows a ring formation on the anodic dielectric [31]. However, the wide deposition of surface electrons is expected, due to the much larger mobility of incident electrons compared to the (positive) ions. The incident electrons are repelled sideways by the already deposited negative surface charges. Again, this correlates with the laterally more extended emission intensity in front of the anode; see (g) in figure 7.

A closer look at figures 10(a) and (b) indicates changes in the positive and negative surface charge distribution during

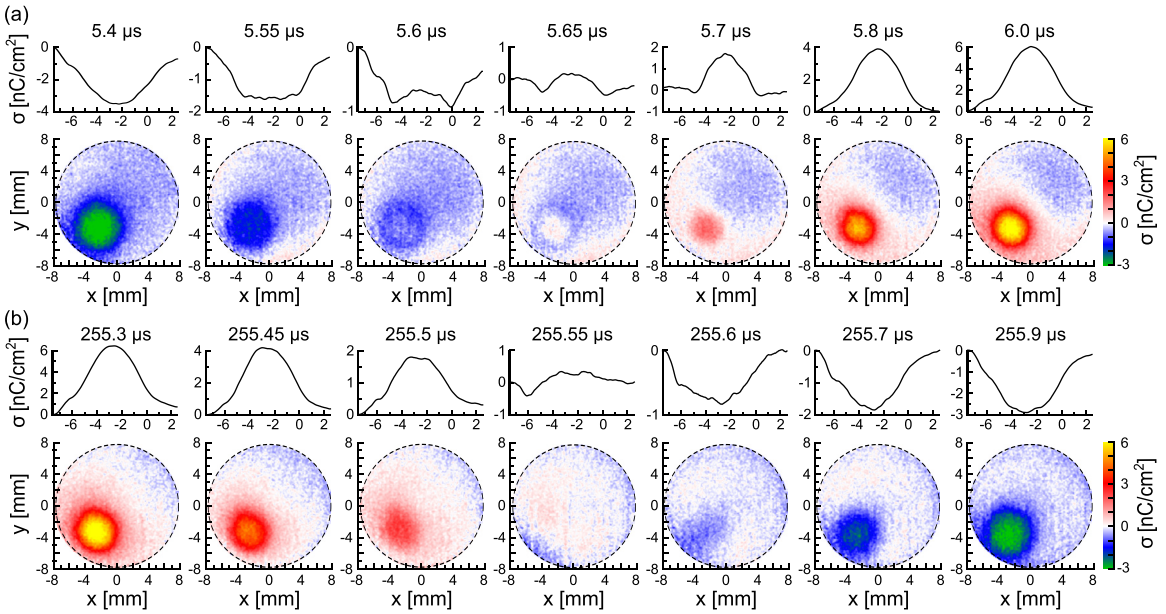

Figure 10. Accumulation of (a) positive surface charges onto the negatively charged cathodic dielectric by incident ions and (b) negative surface charges onto the positively charged anodic dielectric by incident electrons during the breakdown of a single self-stabilized discharge filament. Bottom: 2D spatial surface charge density distribution. Top: 1D profile through the center of the surface charge spot. Operating conditions: He with 10 vol.% N_2, $p = 1$ bar, $\hat{U}_{ext} = 2.2$ kV.

two consecutive discharge breakdowns. These changes result from surface discharges on both dielectrics just after the breakdown in the volume. Figure 11 shows the change in the surface charge density $\Delta\sigma_{cat} = \sigma(t_2) - \sigma(t_1)$ on the cathodic dielectric (b) and $\Delta\sigma_{an} = \sigma(t_4) - \sigma(t_3)$ on the anodic dielectric (c) in between the times t_2 and t_1, and t_4 and t_3, during the respective post-phase highlighted in (a). On the cathodic dielectric (b), $\Delta\sigma_{cat}$ is negative in the center of the surface charge spot and positive in the surrounding ring. This indicates a charge transport in the outward direction and thus the annular propagation of the surface discharge in correlation with the ICCD camera images. In contrast, on the anodic dielectric, $\Delta\sigma_{an}$ is, in general, negative over a large part of the electrode area, however, the change is maximal in the center of the surface charge spot. The wide propagation is due to the much higher mobility of incident electrons compared to ions. Besides, the accumulation in the far surrounding regions may result from electrons that are generated in volume segments beyond the discharge channels. This is indicated by weak optical emission during the breakdown in figure 7.

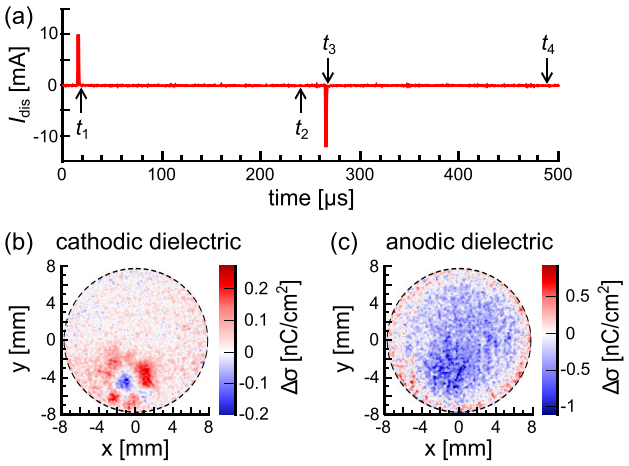

Figure 11. Change in surface charge density distribution due to surface discharges during the post-phase of a single self-stabilized discharge filament: (a) indication of the times t_1, t_2, t_3, and t_4 during the post-phase of both discharge cycles; (b) and (c) difference in surface charge density $\Delta\sigma = \sigma(t_2) - \sigma(t_1)$ and $\Delta\sigma = \sigma(t_4) - \sigma(t_3)$ on the cathodic and anodic dielectric, respectively. He with 10 vol.% N_2, $p = 1$ bar, $\hat{U}_{ext} = 2.2$ kV.

5. Role of memory effects for self-stabilization

5.1. Volume memory effect

Single discharge filaments can be operated for hours at the same position in the present experiment. Note that they are not fixed by the geometry of the discharge configuration, e.g. as done in [12, 13, 15, 16] using semi-spherical electrodes. Consequently, a self-stabilization mechanism exists. First, the focus is on the presence of long-living species that might survive in the volume during consecutive discharge breakdowns and favor the local re-ignition of the discharge, referred to as the volume memory effect. In general, possible candidates are ions in regions with low electric field strength and, especially, metastable states. However, the transit time of ions drifting through the 3 mm gas gap amounts to some microseconds. Note that the gap voltage drop is not as large during the breakdown (see the following section). Moreover, due to the Penning ionization, the effective lifetime of He metastable states decreases to the sub-microsecond time scale in the presence of small nitrogen admixtures in the percentage range. The remaining candidate that might provide a volume memory effect is the metastable $N_2(A^3\Sigma_u^+)$ state.

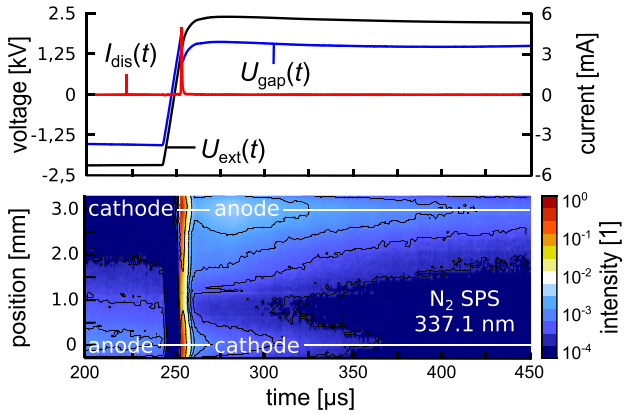

Figure 12. Post-phase of a self-stabilized discharge filament. Top: applied voltage $U_{ext}(t)$, averaged gap voltage $U_{gap}(t)$, and discharge current $I_{dis}(t)$. Bottom: spatio-temporally resolved N_2 SPS emission at 337.1 nm. Operating conditions: He with 10 vol.% N_2, $p = 1$ bar, $\hat{U}_{ext} = 2.5$ kV.

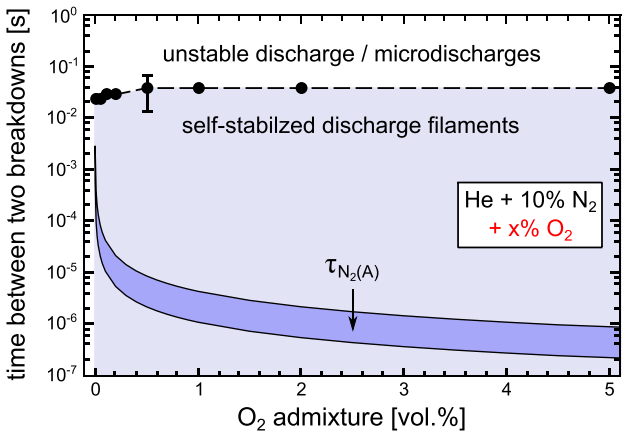

Figure 13. Existence of self-organized and arbitrarily distributed discharge filaments depending on the time interval between two breakdown events in opposite half-cycles of the feeding voltage, and the O_2 admixture to the fixed gas mixture of He with 10 vol.% N_2 at otherwise constant total pressure. In addition, the calculated effective lifetime of the $N_2(A)$ metastable states according to equation 10 is plotted as a function of the O_2 concentration. Operating conditions: $p = 1$ bar, $\hat{U}_{ext} = 2.5$ kV.

In figure 12, the feeding voltage $U_{ext}(t)$, average gap voltage $U_{gap}(t)$ and discharge current $I_{dis}(t)$ as well as the spatio-temporal evolution of the N_2 second positive system (SPS) emission at 337.1 nm are plotted for one half-cycle. Foremost, the excited state $N_2(C^3\Pi_u)$ resulting in the SPS

$$N_2(C^3\Pi_u)_{\nu=0} \rightarrow N_2(B^3\Pi_g)_{\nu'=0} + hc/\lambda_{337.1\ nm} \qquad (7)$$

can be populated by electron-impact excitation from the ground state [12],

$$N_2(X^1\Sigma_g^+) + e^- \rightarrow N_2(C^3\Pi_u) + e^-, \qquad (8)$$

or by the pooling reaction involving metastable states,

$$N_2(A^3\Sigma_u^+) + N_2(A^3\Sigma_u^+) \rightarrow N_2(C^3\Pi_u) + N_2, \qquad (9)$$

with rate coefficient $k_P \approx 3(1) \times 10^{-10}$ cm^3 s^{-1} averaged over the values stated in [43, 44]. Note that other populating channels, including highly excited states, might be relevant too [45]. Most notable in figure 12 is the long-lasting N_2 SPS emission during the post-phase. Especially in front of the anodic dielectric, the SPS emission is detected until the pre-phase of the following discharge breakdown and hence, after the change in feeding voltage polarity, at the new negatively charged cathodic dielectric. If the pooling reaction (9) is the dominant excitation channel during the discharge post-phase, the SPS emission will indicate the presence of metastable $N_2(A^3\Sigma_u^+)$ states. This might favor the local pre-ionization by secondary electron emission [33], and thereby the self-stabilization of the discharge filament.

In order to prove the impact of metastable states on the discharge stability, oxygen was added to the He/N_2 mixture and the time between the two consecutive discharge breakdowns was varied by changing the operating frequency. Figure 13 shows the resulting existence diagram. Surprisingly, there is no remarkable effect of oxygen admixtures on the critical discharge off-time causing the transition to arbitrarily distributed MDs. Without oxygen additives, the effective lifetime $\tau_{N_2(A)} \approx (\sum k_i n_i)^{-1}$ of $N_2(A^3\Sigma_u^+)$ metastable states is strongly determined by the pooling reaction (9) and the quenching by nitrogen with rate coefficient $k_{N_2} = 3 \times 10^{-16}$ cm^{3}s^{-1} [46]. However, in the presence of oxygen, $\tau_{N_2(A)}$ is significantly influenced by the effective quenching reaction

$$N_2(A^3\Sigma_u^+) + O_2 \rightarrow \text{products}, \qquad (10)$$

with rate coefficient $k_{O_2} \approx 3(1) \times 10^{-12}$ cm^3 s^{-1} [44]. The calculated effective lifetime $\tau_{N_2(A)}$ as a function of the O_2 admixture is also plotted in figure 13, for the partial N_2 density $n_{N_2} \approx 2 \times 10^{18}$ cm^{-3} and for the maximum $N_2(A^3\Sigma_u^+)$ density estimated to be in the order of 10^{14} cm^{-3} [33]. Indeed, the starting value $\tau_{N_2(A)} \approx 3$ ms without oxygen additives is uncertain, not least because the quenching by an unknown content of nitrogen atoms is not considered. Note that 3 ms is more than ten times longer than the half-cycle of the feeding voltage. But, even for small O_2 admixtures in the order of 0.1 vol.%, reaction (10) clearly dominates where $\tau_{N_2(A)}$ is reduced by orders of magnitude. This is in contrast to the critical duration between two consecutive discharge breakdowns, determining the stability limit, which keeps approximately constant with the rising oxygen admixture. In conclusion, the volume memory effect by $N_2(A^3\Sigma_u^+)$ metastable states is not crucial for the self-stabilization of discharge filaments. Taking another closer look at the N_2 SPS band emission in figure 12 reveals an exponential increase towards the anode during the post-phase, as well as an abrupt cut-off when the feeding voltage changes its polarity just before the following discharge breakdown. This may indicate the survival of residual electrons in the volume in regions with low electric field.

5.2. Surface memory effect

The critical discharge off-time on the sub-second scale marking the transition to arbitrarily distributed MDs in figure 13 matches with the lifetime of a major surface charge population, as experimentally shown in [28, 32]. Hence, the residual

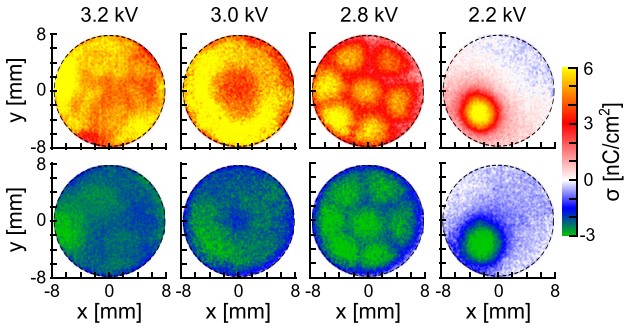

Figure 14. 2D distribution of positive and negative surface charges for the filamentary discharge in He with 10 vol.% N_2 at $p = 1$ bar, driven by different feeding voltage amplitudes.

surface charge is the most probable candidate providing the self-stabilization of discharge filaments. As discussed in section 3, a reduction of the feeding voltage amplitude from 3.2 kV to 2.2 kV causes the transition from arbitrarily distributed MDs to the rotating and stable filament pattern, ending up with a single self-stabilized discharge filament. This is illustrated in figure 14, based on the two-dimensional distribution of positive and negative surface charges for the filamentary BD in He with 10 vol.% N_2 admixture at a total pressure of 1 bar. Each image is averaged over several feeding voltage cycles. That is why the arbitrary re-ignition of MDs (3.2 kV) and the rotating re-ignition of patterned discharge filaments (3.0 kV) are indicated by overlapped spots and a ring, respectively. In between the hexagonal filament pattern (2.8 kV) and the single filament (2.2 kV), the arrangements of four, three and two filaments can be observed. The difference in feeding voltage amplitude of 1 kV for the initial discharge ignition in the MD regime and the operation of a single discharge filament must be compensated by the additional electric field at the positions of the surface charge spots. This is referred to as the surface memory effect.

For quantitative evidence, the spatio-temporally resolved gap voltage $U_{gap}(x, y, t)$ was recalculated with equation (5). Figure 15 illustrates the 2D gap voltage distribution just before the breakdown of a single self-stabilized discharge filament in (a) and the gap voltage dynamics in the center of the surface charge spot and at the edges in (b). The discharge current pulse $I_{dis}(t)$ indicates the breakdown phase. Both the externally applied voltage $U_{ext}(t)$ and the surface charge density $\sigma_{sur}(x, y, t)$ determine the dynamics of the gap voltage. As visible in (a), the surface charge spot significantly contributes to the spatial gap voltage distribution. The required breakdown voltage of about 2.7 kV is only reached at the center of a surface charge spot, whereas, in the surrounding regions where no surface charges were accumulated, the gap voltage is close to 1.6 kV. This value equals the partial feeding voltage drop across the gas gap. Hence, the difference in the feeding voltage of about 1 kV between the operation of the single self-stabilized discharge filament and the MD regime is compensated by the surface charge exclusively at a well-localized position. As the partial feeding voltage drop never reaches the required breakdown voltage at any time, no further discharge events take place. Thus, the local electric field enhancement by surface charges causes the periodic re-ignition of the discharge

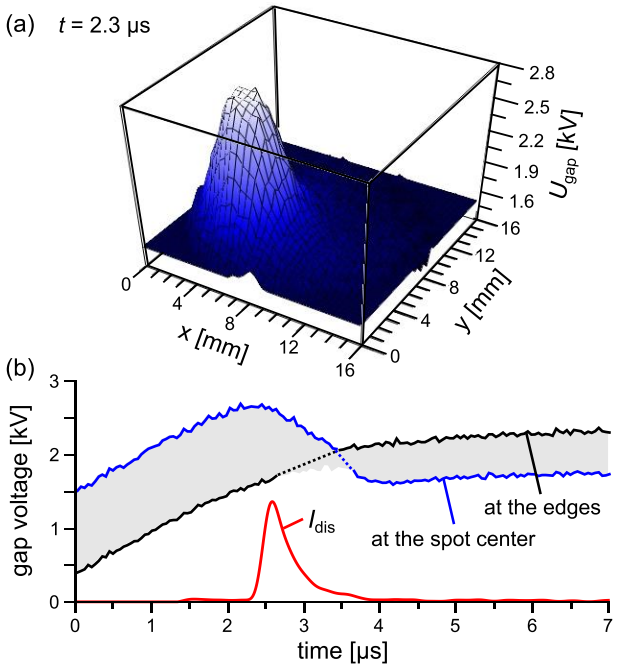

Figure 15. Gap voltage during the development of a single self-stabilized discharge filament: (a) spatial gap voltage distribution calculated with equation (5) just before the discharge breakdown at $t = 2.3$ μs, and (b) gap voltage dynamics in the center of the surface charge spot and in the surrounding regions. Operating conditions: He with 10 vol.% N_2, $p = 1$ bar, $\hat{U}_{ext} = 2.2$ kV.

filament at the same position. But, when the feeding voltage is increased again, the surface charge spots at the footprints of several discharge filaments are not well-separated anymore, and the breakdown voltage is reached at later times in between the positions of the initial discharge filaments too. As a result, the conservation of the lateral discharge structure gets lost. To summarize, the surface memory effect is the key mechanism behind the self-stabilization of discharge filaments in the plane-parallel electrode configuration.

6. Conclusion

The presented paper reports on the formation of a single self-stabilized discharge filament in a plane-parallel barrier discharge configuration. The discharge was operated by square-wave feeding voltage in He/N_2 mixtures at variable pressures. For the first time, the combined application of optical diagnostics and surface charge diagnostics on a filamentary breakdown allowed the correlation between the discharge development in the volume and on the dielectric surfaces.

The existence regimes of the self-stabilized discharge filaments were obtained by systematic variation of the N_2 admixture of maximal 50 vol.% to He, total pressure between 100 mbar and 1 bar and thus a feeding voltage amplitude between 0.3 kV and 3.5 kV. In fact, a single self-stabilized discharge filament can be operated over a wide range of total pressure and He/N_2 mixture, with a required minimum N_2 admixture of about 0.2 vol.%. This proves the independence of the self-stabilization mechanism from specific properties

of the gas system. In general, the stable discharge filament is obtained by a significant reduction of the feeding voltage amplitude after the initial ignition in the microdischarge regime. The voltage interval allowing the stable operation of discharge filaments increases with the rising total pressure and N_2 admixture to He, which is connected with an increase in the amount of the transported and subsequently deposited charge. This is the first indication of the self-stabilization of the discharge filament being caused by the local surface charge distribution.

Indeed, residual surface charges on the dielectrics significantly contribute to the gap voltage distribution. In the case of a single self-stabilized discharge filament, the required gap voltage of about 2.7 kV for the discharge breakdown is only reached at the center of the surface charge spot. But, in the surrounding regions where no surface charges were accumulated, the gap voltage is more than 1 kV lower. As long as the surface charge spots of several discharge filaments are well-separated, the local enhancement of the electric field conserves the long-term stability of the lateral discharge structure. Vice versa, the enhancement of the voltage amplitude causes a transition to the rotating filament patterns and, finally, to the arbitrarily distributed MDs. The required breakdown voltage is then also reached in between the initial filament positions. Contrary to the outstanding importance of the surface memory effect, the volume memory effect by $N_2(A^3\Sigma_u^+)$ metastable states is not crucial. There was no notable influence of the oxygen concentration on the discharge stability, despite the effective quenching of $N_2(A^3\Sigma_u^+)$ by oxygen.

Finally, the spatio-temporal evolution of the single self-stabilized discharge filament reveals similarities to both microdischarges and the glow-like discharge. The main characteristics, in chronological order, are the Townsend pre-phase of some μs duration, the cathode-directed ionization front propagating on the ns time scale, the negative glow in front of the cathode followed by Faraday dark space, the positive column and the anode glow at the moment of maximum discharge current, as well as the long-lasting afterglow in the discharge channel and radially spreading surface discharges on the dielectrics during the post-phase. Additionally, the intensity ratio of He single lines as a qualitative measure of the local electric field indicates a cathode fall with an axial extent of 0.1 mm. Hence, the optical diagnostics reveal the breakdown mechanism to be determined by space charge formation and significant electric field distortion across the gas gap. The constricted cathode-directed ionization front correlates with the centered formation of positive surface charges during the breakdown. In addition, the radial propagation of the surface discharges on both dielectrics could be correlated with the annular change in surface charge density during the post-phase.

In order to measure the fast ionization front, a square-wave voltage with a shorter rise time should be used to reduce the temporal jitter of the discharge. The single self-stabilized discharge filament provides the possibility to determine the spatio-temporal evolution of the electric field by the measured He singlet line intensity ratio in combination with a collision-radiation model. In this context, it would be interesting to vary the He/N_2 mixing ratio, as well as the gas gap width, in order to investigate the transition regime to the well-known glow-like barrier discharge. Moreover, it is planned to measure the morphology and lifetime of surface charges in correlation with the self-stabilization of discharge filaments under systematic variation of the gas system including various gases.

Acknowledgments

The presented work was supported by the Deutsche Forschungsgemeinschaft through the Project No. B11 of the Collaborative Research Center Transregio 24 (TRR 24), ‘Fundamentals of Complex Plasmas’.

References

[1] Kanazawa S, Kogoma M, Moriwaki T and Okazaki S 1988 Stable glow plasma at atmospheric pressure *J. Phys. D: Appl. Phys.* **21** 838–40
[2] Okazaki S, Kogoma M, Uehara M and Kimura Y 1993 Appearance of stable glow discharge in air, argon, oxygen and nitrogen at atmospheric pressure using a 50 Hz source *J. Phys. D: Appl. Phys.* **26** 889–92
[3] Massines F, Rabehi A, Decomps P, Ségur P, Ben Gadri R and Mayoux C 1998 Experimental and theoretical study of a glow discharge at atmospheric pressure controlled by dielectric barrier *J. Appl. Phys.* **83** 2950–57
[4] Siemens W 1857 Poggendorff’s *Ann. Phys. Chem.* **102** 66
[5] Eliasson B, Hirth M and Kogelschatz U 1987 Ozone synthesis from oxygen in dielectric barrier discharges *J. Phys. D: Appl. Phys.* **20** 1421–37
[6] Samoilovich V G, Gibalov V I and Kozlov K V 1997 *Physical Chemistry of the Barrier Discharge* (Düsseldorf: DVS)
[7] Kogelschatz U 2003 Dielectric-barrier discharges: their history, discharge physics, and industrial applications *Plasma Chem. Plasma Process.* **23** 1–46
[8] Becker K H, Kogelschatz U, Schoenbach K H and Barker R J 2004 *Non-Equilibrium Air Plasmas at Atmospheric Pressure* (*Series in Plasma Physics*) (Bristol: Institute of Physics Publishing)
[9] Wagner H-E, Brandenburg R, Kozlov K V, Sonnenfeld A, Michel P and Behnke J F 2003 The barrier discharge: basic properties and applications to surface treatment *Vacuum* **71** 417–36
[10] Fridman G, Friedman G, Gutsol A, Shekhter A B, Vasilets V N and Fridman A 2008 Applied plasma medicine *Plasma Process. Polym.* **5** 503–33
[11] Kozlov K V, Shepeliuk O and Samoilovich V 1995 Spatio-temporal evolution of the dielectric barrier discharge channels in air at atmospheric pressure *Proc. 11th Int. Conf. on Gas Discharges and their Applications (Tokyo, Japan)* vol 2 pp 79–83
[12] Kozlov K V, Wagner H-E, Brandenburg R and Michel P 2001 Spatio-temporally resolved spectroscopic diagnostics of the barrier discharge in air at atmospheric pressure *J. Phys.* D **34** 3164–76
[13] Wagner H-E, Brandenburg R and Kozlov K V 2004 Progress in the visualization of filamentary gas discharges, Part 1: milestones and diagnostics of dielectric-barrier discharges by cross-correlation spectroscopy *J. Adv. Oxid. Technol.* **7** 11–9
[14] Heuser C and Pietsch G 1980 Pre-breakdown phenomena between glass-glass and metal-glass electrodes *Proc. 6th Int. Conf. on Gas Discharges and their Applications (Edinburgh, UK)* 98–101

[15] Hoder T, Höft H, Kettlitz M, Weltmann K-D and Brandenburg R 2012 Barrier discharges driven by sub-microsecond pulses at atmospheric pressure: breakdown manipulation by pulse width *Phys. Plasmas* **19** 070701
[16] Höft H, Kettlitz M, Becker M M and Weltmann K-D 2014 Breakdown characteristics in pulsed-driven dielectric barrier discharges: Influence of the pre-breakdown phase due to volume memory effects *J. Phys. D: Appl. Phys.* **47** 465206
[17] Eliasson B, Kogelschatz U and Hirth M 1985 The Townsend/streamer transition in a silent discharge in oxygen *Proc. XVII In. Conf. on Phenomena in Ionized Gases (Budapest, Hungary)* pp 590–2
[18] Braun D, Gibalov V and Pietsch G 1992 Two-dimensional modelling of the dielectric barrier discharge in air *Plasma Sources Sci. Technol.* **1** 166–74
[19] Xu X and Kushner M J 1998 Multiple microdischarge dynamics in dielectric barrier discharges *J. Appl. Phys.* **84** 4153–60
[20] Yurgelenas Y V and Wagner H-E 2006 A computational model of a barrier discharge in air at atmospheric pressure: the role of residual surface charges in microdischarge formation *J. Phys. D: Appl. Phys.* **39** 4031–43
[21] Li M, Li C, Zhan H and Xu J 2008 Effect of surface charge trapping on dielectric barrier discharge *Appl. Phys. Lett.* **92** 031503
[22] Ambrico P F, Ambrico M, Colaianni A, Schiavulli L, Dilecce G and De Benedictis S 2010 Thermoluminescence study of the trapped charge at alumina surface electrode in different dielectric barrier discharges regimes *J. Phys. D: Appl. Phys.* **43** 325201
[23] Ambrico P F, Ambrico M, Schiavulli L and De Benedictis S 2014 2D Thermoluminescence imaging of dielectric surface long term charge memory of plasma surface interaction in DBD discharges *J. Phys. D: Appl. Phys.* **47** 305201
[24] Kawasaki T, Tereashima T, Zhu Y, Takada T and Maeno T 1994 Highly sensitive measurement of surface charge distribution using the pockels effect and an image lock-in amplifier *J. Phys. A: Appl. Phys.* **27** 1646–52
[25] Sugimoto K, Takahashi H, Shimomura O and Sakurai T 2003 Measurement of wall voltage in barrier discharges using an electro-optic nonlinear crystal *J. Phys. D: Appl. Phys.* **36** 2887–90
[26] Jeong D C, Bae H S and Whang K W 2005 Measurement of the spatiotemporal surface charge distribution in an ac plasma display cell using pockels effect *J. Appl. Phys.* **97** 013304
[27] Bogaczyk M, Wild R, Stollenwerk L and Wagner H-E 2012 Surface charge accumulation and discharge development in diffuse and filamentary barrier discharges operating in He, N_2 and mixtures *J. Phys. D: Appl. Phys.* **45** 465202
[28] Tschiersch R, Bogaczyk M and Wagner H-E 2014 Systematic investigation of the barrier discharge operation in helium, nitrogen, and mixtures: discharge development, formation and decay of surface charges *J. Phys. D: Appl. Phys.* **47** 365204
[29] Tschiersch R, Nemschokmichal S, Bogaczyk M and Meichsner J 2017 Surface charge measurements on different dielectrics in diffuse and filamentary barrier discharges *J. Phys. D: Appl. Phys.* **50** 105207
[30] Stollenwerk L, Laven J G and Purwins H-G 2007 Spatially resolved surface-charge measurement in a planar dielectric-barrier discharge system *Phys. Rev. Lett.* **98** 255001
[31] Wild R and Stollenwerk L 2014 Phase-resolved measurement of the spatial surface charge distribution in a laterally patterned barrier discharge *New J. Phys.* **16** 113040
[32] Wild R, Benduhn J and Stollenwerk L 2014 Surface charge transport and decay in dielectric barrier discharges *J. Phys. D: Appl. Phys.* **47** 435204
[33] Nemschokmichal S and Meichsner J 2015 Spatio-temporal characterization of $N_2(A^3\Sigma_u^+)$ metastables in diffuse nitrogen barrier discharge *J. Phys. D: Appl. Phys.* **48** 405203
[34] Brauer I, Pusent C, Purwins H-G and Boeuf J P 1999 Simulation of self-organized filaments in a dielectric barrier glow discharge plasma *J. Appl. Phys.* **85** 7569–72
[35] Guaitella O, Marinov I and Rousseau A 2011 Role of charge photodesorption in self-synchronized breakdown of surface streamers in air at atmospheric pressure *Appl. Phys. Lett.* **98** 071502
[36] Lee F W and Collins C B 1976 Measurement of the rate coefficients for the bimolecular and termolecular deexcitation reactions of $He(2^3S)$ with Ne, Ar, N_2, CO, CO_2, and CH_4^* *J. Chem. Phys.* **65** 5189–97
[37] Martens T and Bogaerts A 2008 The dominant role of impurities in the composition of high pressure noble gas plasmas *Appl. Phys. Lett.* **92** 041504
[38] Šimek M, Ambrico P F and Prukner V 2011 ICCD microscopic imaging of a single micro-discharge in surface coplanar DBD geometry: determination of the luminous diameter of N_2 and Ar streamers *Plasma Sources Sci. Technol.* **20** 025010
[39] Massines F, Sègur P, Gherardi N, Khamphan C and Ricard A 2003 Physics and chemistry in a glow dielectric barrier discharge at atmospheric pressure: diagnostics and modelling *Surf. Coat. Technol.* **174-175** 8–14
[40] Ivković S S, Sretenović G B, Obradović B M, Cvetanović N and Kuraica M M 2014 On the use of the intensity ration of He lines for electric field measurements in atmospheric pressure dielectric barrier discharge *J. Phys. D: Appl. Phys.* **47** 055204
[41] Tschiersch R, Nemschokmichal S and Meichsner J 2017 Influence of released surface electrons on the pre-ionization of helium barrier discharges: Laser photodesorption experiment and 1D fluid simulation *Plasma Sources Sci. Technol.* **26** 075006
[42] Stollenwerk L and Stroth U 2011 Electric charging in dielectric barrier discharges with asymmetric gamma-coefficients *Contrib. Plasma Phys.* **51** 61–7
[43] Piper L G 1988 State-to-state $N_2(A^3\Sigma_u^+)$ energy-pooling reactions I. The formation of $N_2(C^3\Pi_u)$ and the Herman infrared systems *J. Chem. Phys.* **88** 231–9
[44] Herron J T 1999 Evaluated chemical kinetics data for reactios of $N(^2D)$, $N(^2P)$, and $N_2(A^3\Sigma_u^+)$ in the gas phase *J. Chem. Phys. Ref. Data* **28** 1453–83
[45] Šimek M, Ambrico P F, De Benedictis S, Dilecce G, Prukner V and Schmidt J 2010 $N_2(A^3\Sigma_u^+)$ behaviour in a N_2–NO surface dielectric barrier discharge in the modulated ac regime at atmospheric pressure *J. Phys. D: Appl. Phys.* **43** 124003
[46] Cartry G, Magne L and Cernogora G 1999 Experimental study and modeling of a low-pressure N_2–O_2 time afterglow *J. Phys. D: Appl. Phys.* **32** 1894–7